



American Society of  
Mechanical Engineers

## ASME Accepted Manuscript Repository

### Institutional Repository Cover Sheet

**ASME Paper Title:**

Analysis of Transonic Bladerows With Non-Uniform Geometry Using the Spectral Method

**Authors:**

Feng Wang and Luca di Mare

**ASME Journal Title:**

Journal of Turbomachinery

**Volume/Issue:**

143/12

**Date of Publication (VOR\* Online):**

27 July 2021

**ASME Digital Collection URL:**

<https://asmedigitalcollection.asme.org/turbomachinery/article/143/12/121012/1114412/Analysis-of-Transonic-Bladerows-With-Non-Uniform>

**DOI:**

<https://doi.org/10.1115/1.4051710>

\*VOR (version of record)

# ANALYSIS OF TRANSONIC BLADEROWS WITH NON-UNIFORM GEOMETRY USING SPECTRAL METHOD

**Feng Wang\***

Oxford Thermo-Fluids Institute  
Department of Engineering Science  
University Of Oxford  
UK  
feng.wang@eng.ox.ac.uk

**Luca di Mare**

Oxford Thermo-Fluids Institute  
Department of Engineering Science  
University Of Oxford  
UK

## ABSTRACT

*Turbomachinery blade rows can have non-uniform geometries due to design intent, manufacture errors or wear. When predictions are sought for the effect of such non-uniformities, it is generally the case that whole assembly calculations are needed. A spectral method is used in this paper to approximate the flow fields of the whole assembly but with significantly less computation cost. The method projects the flow perturbations due to the geometry non-uniformity in an assembly in Fourier space, and only one passage is required to compute the flow perturbations corresponding to a certain wave-number of geometry variation. The performance of this method on transonic blade rows is demonstrated on a modern fan assembly. Low engine order and high engine order geometry non-uniformity (e.g. “saw-tooth” pattern) are examined. The non-linear coupling between the flow perturbations and the passage-averaged flow field is also demonstrated. Pressure variations on the blade surface and the potential flow field upstream of the leading edge from the proposed spectral method and the direct whole assembly solutions are compared. Good agreement is observed on both quasi-3D and full 3D cases. A lumped approach to compute deterministic fluxes is also proposed to further reduce the computational cost of the spectral method. The spectral method is formulated in such a way that it can be easily implemented into an existing harmonic flow solver by adding an extra source term, and can be potentially used as an efficient tool for aeromechanical and aeroacoustics design of turbomachinery blade rows.*

## Introduction

Computational Fluid Dynamics (CFD) has become an indispensable element in turbomachinery design and analysis. Despite the advances in computer hardware, three-dimensional (3D) viscous simulations of the whole assembly of a blade row are still considered too expensive to be routinely included in an iterative design process. Low fidelity models (e.g. panel methods using potential flow theory) based on reduced forms of the Navier-Stokes (NS) equations can be used instead to analyse large volumes of design in a timely manner. Nonetheless, there has been a growing need from the industry to include more fidelity into the design tools to enhance design confidence without significantly increasing the computational cost. Therefore a reduced model is normally required to capture the dominant feature of the flow field but demand much less computational cost compared to the full model.

In turbomachinery CFD, spectral methods are popular approaches for simulating periodic unsteady flows. The strategy is to project the time-domain unsteady NS equations onto the Fourier space. Such projection turns the time-domain unsteady flow problem into a steady problem in Fourier space, so that the full armory of convergence acceleration methods can be applied with advantage. Additionally, for multistage simulations, phase shift can be applied at the periodic boundaries so that only one passage is required. For a typical multistage URANS simulation, the wall-clock time can be reduced by 1 to 3 orders of magnitude compared to direct unsteady simulations of the whole annulus domain.

Hall et al [1] used a linearized Euler approach to compute unsteady flows for turbomachinery cascades. He and Ning [2] coupled the linearized NS solver and the mean flow via deterministic stresses [3]. This method is termed as the Non-Linear Harmonic (NLH) method. The original NLH was formulated with time-averaged conservative variables, and a Favre-averaged formulation of NLH was recently proposed by Wang and di Mare [4] to allow minimum modifications to implement NLH into an existing CFD solver. Hall et al [5] devised the Harmonic Balance (HB) method to consider the couplings of the harmonics. There were a few variants of the HB methods, such as the non-linear frequency domain method [6] and the time spectral method [7]. It is noted that mathematically these variants are essentially similar and it is a matter of preference of storing the flow variables as Fourier coefficients or time-level form [8]. Finally, cross-coupling of the harmonics can also be realized in NLH to improve its performance in flows with strong non-linearity, readers can refer to [9–11] for more details. There has been extensive research on the spectral method for unsteady flows and the interested reader can refer to the review papers by He [12] and Hall et al [8] for more information.

Spectral methods are typically designed for unsteady flows, but there is very limited research on how to apply the spectral method to handle geometry complexity. He [13] developed an interesting spectral method to deal with flow variations in space for the secondary air system and Outlet Guide Vane (OGV) - pylon interactions, but in He's work no geometry variations were considered.

Wang and di Mare [14] recently devised a spectral method to efficiently compute flow fields in an assembly with non-uniform geometries. The method projected the geometry distortions in the assembly onto the Fourier space and the flow perturbation related to each mode of the geometry variation is computed. The final flow field is produced by linear combination of the solution of each mode. The method has been successfully applied to an OGV assembly by reducing the computational cost by at least one order of magnitude

compared to the equivalent whole-annulus RANS simulation.

For large and flexible blades, such as the fans of large civil turbofans, the determination of the running shape of the assembly and the determination of bounds of the likely geometric variability in service is an important aspect of the design process. The blade-to-blade geometry variability can lead to performance degradation [15], aerodynamic excitation [16], improve flutter stability [17], and generate buzz-saw noise [18–20]. Fan blades in static conditions can have different geometries due to manufacture tolerance and operation wear. Fan blades untwist significantly during operation and their precise configuration at a given condition is affected by small details of their cold shape which affect their performance and their untwist characteristics. Wilson et al [15] showed the extent to which untwist can lead to the formation of patterns in fan assemblies, such as the “saw-tooth” pattern (e.g. Fig. 11). The aero-elastic issue of the “saw-tooth” on the fan blade vibration is revised recently by Lu et al [21] and the underlying mechanism is also studied.

Previous researches on the fan assembly with non-uniform geometries normally require the whole assembly to be simulated. There is a need to allow effects of geometry asymmetry in a fan assembly to be assessed efficiently in design and analysis. This work is to address this need and the contribution of this work is to

- Demonstrate the performance of the spectral method to predict the flow fields in fan passages under low and high engine order geometry distortions.
- Study comparatively of the variants of the spectral method and demonstrate their performance with difference levels of flow non-linearity.
- Propose a lumped approach to compute deterministic fluxes to further reduce computational cost of the spectral method.

This paper is organized as the following: the mathematical formulation of the spectral method is briefly introduced in the first place, the general procedure of the method is pictured, and its computational cost is discussed. The performance of the method is demonstrated on low EO geometry distortions and fan blades with the “saw-tooth” pattern in quasi-3D and full 3D simulations. Finally the paper is concluded and future improvement of the method is also pointed out.

## Methodology

### Spectral Formulation of Flow Perturbations in An Assembly with Non-Uniform Geometry

The spectral method is briefly described below and more details can be found in Wang and di Mare [14]. The strategy is to firstly establish the relation between grid displacement and flow perturbation for a single passage. The formulation is then extended to an assembly of components and finally projected to the Fourier space.

Assume there are two numerical setups for a blade passage. Both cases have identical boundary conditions and mesh topology, but the coordinates of the nodes in both meshes differ slightly due to a minor change (e.g. blade rotation) in the geometry of the second case.

Let the grid coordinates and converged steady-state solutions for both cases be denoted as  $(\mathbf{x}, \mathbf{U})$  and  $(\mathbf{x}^*, \mathbf{U}^*)$ , respectively, the

residuals of these two converged steady state solutions can be written as:

$$\mathbf{R}(\mathbf{x}, \mathbf{U}) = \mathbf{0} \quad \text{1st setup, baseline} \quad (1)$$

$$\mathbf{R}(\mathbf{x}^*, \mathbf{U}^*) = \mathbf{0} \quad \text{2nd setup, with geometry change} \quad (2)$$

If we denote the difference of the coordinates and flow solutions between these two meshes as:

$$\Delta \mathbf{x} = \mathbf{x}^* - \mathbf{x} \quad (3)$$

$$\Delta \mathbf{U} = \mathbf{U}^* - \mathbf{U} \quad (4)$$

Expanding  $\mathbf{R}(\mathbf{x}^*, \mathbf{U}^*)$  with Taylor series and ignoring the high order terms, we can obtain:

$$\mathbf{R}(\mathbf{x}^*, \mathbf{U}^*) = \mathbf{R}(\mathbf{x}, \mathbf{U}) + \left. \frac{\partial \mathbf{R}}{\partial \mathbf{x}} \right|_{(\mathbf{x}, \mathbf{U})} \Delta \mathbf{x} + \left. \frac{\partial \mathbf{R}}{\partial \mathbf{U}} \right|_{(\mathbf{x}, \mathbf{U})} \Delta \mathbf{U} \quad (5)$$

Since  $\mathbf{R}(\mathbf{x}^*, \mathbf{U}^*) = \mathbf{0}$  and  $\mathbf{R}(\mathbf{x}, \mathbf{U}) = \mathbf{0}$ , Equation 5 can be rewritten as:

$$\left. \frac{\partial \mathbf{R}}{\partial \mathbf{U}} \right|_{(\mathbf{x}, \mathbf{U})} \Delta \mathbf{U} = - \left. \frac{\partial \mathbf{R}}{\partial \mathbf{x}} \right|_{(\mathbf{x}, \mathbf{U})} \Delta \mathbf{x} \quad (6)$$

Equation 6 shows the *linear correlation* between grid displacement and flow perturbation. This can be easily expanded for an assembly of passages if we assume the baseline mesh and baseline solution in Equation 3 are the mesh for the passage-averaged or nominal geometry and the passage-averaged solution, respectively. The linear correlation for passage k reads:

$$\left. \frac{\partial \mathbf{R}}{\partial \mathbf{U}} \right|_{(\bar{\mathbf{x}}, \bar{\mathbf{U}})} \Delta \mathbf{U}_k = - \left. \frac{\partial \mathbf{R}}{\partial \mathbf{x}} \right|_{(\bar{\mathbf{x}}, \bar{\mathbf{U}})} \Delta \mathbf{x}_k \quad (7)$$

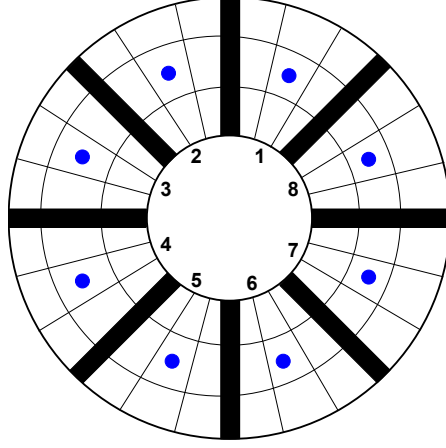


**FIGURE 1.** Schematic of the spatial Fourier transform of  $\mathbf{G}_k$ . The cells highlighted by the blue dots are the ones that are used for the spatial Fourier transform.

$\bar{\mathbf{U}}$  is the passage averaged flow fields on the mesh of the passage-averaged geometry  $\bar{\mathbf{x}}$ .  $\bar{\mathbf{U}}$  is defined as:

$$\bar{\mathbf{U}} = \frac{1}{N} \sum_{k=1}^{k=N} \mathbf{U}_k \quad (8)$$

$k$  is the passage index and  $N$  is the number of passages in the assembly. The flow perturbation  $\Delta \mathbf{U}_k$  is defined as  $\Delta \mathbf{U}_k = \mathbf{U}_k - \bar{\mathbf{U}}$ . The grid displacement  $\Delta \mathbf{x}_k$  is defined as  $\Delta \mathbf{x}_k = \mathbf{x}_k - \bar{\mathbf{x}}$ .  $\mathbf{U}_k$  and  $\mathbf{x}_k$  are the solutions and the grid points of the  $k$ th passage of the assembly.

It is noted that the linearization is applied on  $\bar{\mathbf{U}}$  and  $\bar{\mathbf{x}}$ , therefore they are independent from the passage index  $k$ . In the following text, for simplicity,  $-\frac{\partial \mathbf{R}}{\partial \mathbf{x}}|_{(\bar{\mathbf{x}}, \bar{\mathbf{U}})} \Delta \mathbf{x}_k$  is represented by the symbol  $\mathbf{G}_k$ . Since  $\Delta \mathbf{x}_k$  is already known,  $\mathbf{G}_k$  can be computed using finite difference by ignoring the high order terms, this reads:

$$\mathbf{G}_k = \mathbf{R}_k(\mathbf{x}_k, \bar{\mathbf{U}}) - \mathbf{R}_k(\bar{\mathbf{x}}, \bar{\mathbf{U}}) \quad (9)$$

The linear formulation which connects grid displacement and flow perturbation in passage  $k$  then reads:

$$\frac{\partial \mathbf{R}}{\partial \mathbf{U}} \bigg|_{(\bar{\mathbf{x}}, \bar{\mathbf{U}})} \Delta \mathbf{U}_k = \mathbf{G}_k \quad (10)$$

Equation 10 is in the physical space and  $\bar{\mathbf{U}}$  and  $\bar{\mathbf{x}}$  is independent from the passage index  $k$ . Assume the grid displacement is made of a few Fourier modes, a spatial Fourier transform of Equation 10 will produce the flow perturbations with respect to a certain Fourier mode of the grid displacement in the Fourier space.

The spatial Fourier transform is computed in the following way: since each passage has identical mesh connectivity, the  $i^{th}$  cell of each passage has unique corresponding cells in other passages, which is illustrated in Fig. 1. If the Fourier transform of the  $i^{th}$  cell of  $\mathbf{G}_k$  is to be computed, the Fourier transform  $\mathcal{F}(\mathbf{G}_k^i)$  is applied on the data set  $\mathbf{G}_k^i$ , which consists of:

$$\{\mathbf{G}_k^i\} = \{\mathbf{G}_1^i, \mathbf{G}_2^i, \dots, \mathbf{G}_N^i\} \quad (11)$$

Where  $k$  is the passage index. The Fourier transform for the flow perturbations  $\mathcal{F}(\Delta \mathbf{U}_k^i)$  are conducted in an identical fashion. It is also noted that the spatial Fourier transform is performed on the node or cell index, therefore a uniform sampling always hold. Without losing generality, if the  $l^{th}$  harmonic of the grid displacement is considered, the resulting formulation reads:

$$\left. \frac{\partial \mathbf{R}}{\partial \mathbf{U}} \right|_{(\bar{\mathbf{x}}, \bar{\mathbf{U}})} \hat{\mathbf{U}}_l = \hat{\mathbf{G}}_l \quad (12)$$

$l$  is the harmonic index,  $\hat{\mathbf{U}}_l$  is the  $l^{th}$  harmonic of  $\mathcal{F}(\mathbf{U}_k)$ .  $\hat{\mathbf{G}}_l$  is the  $l^{th}$  harmonic of  $\mathcal{F}(\mathbf{G}_k)$ . It is noted that Equation 12 is in the Fourier space and it only requires  $\bar{\mathbf{U}}$  and  $\bar{\mathbf{x}}$ . This means only one passage is required to compute  $\hat{\mathbf{U}}_l$ .

Equation 12 shows the relationship between grid displacement and flow perturbation in the spectral or Fourier space. It is more convenient to add a pseudo time  $t^*$  on its left hand side, as is shown in Equation 13, so that it can be solved with classical iterative techniques for steady state problems.

$$\frac{\partial \hat{\mathbf{U}}_l}{\partial t^*} + \left. \frac{\partial \mathbf{R}}{\partial \mathbf{U}} \right|_{(\bar{\mathbf{x}}, \bar{\mathbf{U}})} \hat{\mathbf{U}}_l = \hat{\mathbf{G}}_l \quad (13)$$

### Computation of Passage-Averaged Flow

For an assembly with geometry non-uniformity, the flow field can be decomposed as a passage-averaged mean and flow perturbations, which is caused by geometry variations. The previous section has described how to compute the flow perturbations and assume

the passage-averaged flow is available. In this section we describe how to define and compute the mean flow.

For a steady-state solution, the passage-averaged flow is governed by the following equation:

$$\overline{\mathbf{R}(\mathbf{U})} = \mathbf{R}(\bar{\mathbf{U}}) + \mathbf{DF} = 0 \quad (14)$$

Equation 14 is similar to the one for time-mean flow (see He [22]), but here the mean flow is passage-averaged.  $\overline{\mathbf{R}(\mathbf{U})}$  is the passage-averaged residual and it has two contributions. The first one is the one computed using the passage-averaged flow variables and the extra term in Equation 14 is the passage-averaged Deterministic Flux (DF) [3]. The presence of this term is due to the non-linearity of the Navier-Stokes equations. Due to the existence of this term,  $\bar{\mathbf{U}}$  is different from the single passage solution.

As demonstrated by Wang and di Mare [4], it is more convenient to work with Favre-averaged variables for compressible flows. The passage-averaged flow field can be defined via a dummy variable  $\phi$  as;

$$\begin{aligned} \bar{\phi} &= \frac{1}{N} \sum_{k=1}^{k=N} \phi_k \\ \tilde{\phi} &= \frac{\bar{\rho\phi}}{\bar{\rho}} \end{aligned} \quad (15)$$

$k$  is passage index and  $N$  is number of passages in the assembly. The bar “—” represents passage averaging and the tilde “ $\sim$ ” Favre-averaging or density averaging. Accordingly, the variation of a variable  $\phi$  to the passage-mean or Favre-averaged value can be defined as:

$$\begin{aligned} \phi' &= \phi - \bar{\phi} \\ \phi'' &= \phi - \tilde{\phi} \end{aligned} \quad (16)$$

With the above definition, DF in the passage-averaged momentum and energy convective fluxes can be written as:



$$\begin{aligned}
\overline{\rho u_i u_j + p} &= \underbrace{\bar{\rho} \tilde{u}_i \tilde{u}_j}_{\text{mean flow}} + \underbrace{\overline{\rho u_i'' u_j''}}_{\text{DF}} \\
\overline{\rho u_i \bar{H}} &= \underbrace{\bar{\rho} \tilde{u}_i \tilde{H}}_{\text{mean flow}} + \underbrace{\overline{\rho u_i'' H''}}_{\text{DF}}
\end{aligned} \tag{17}$$

$\overline{\rho u_i'' u_j''}$  and  $\overline{\rho u_i'' H''}$  are passage-averaged deterministic fluxes. The variation with superscript  $''$  represents the variation with respect to its Favre-averaged value. It is also noted that in the energy equation, the work done by the shear stresses can be decomposed as:

$$\overline{\tau_{ij} u_j} = \underbrace{\bar{\tau}_{ij} \tilde{u}_j}_{\text{mean flow}} + \underbrace{\overline{\tau_{ij}'' u_j''}}_{\text{DF}} \tag{18}$$

From our experience, it is found that DF in the convective fluxes have a dominant effect over the one related to the shear stress. For a complete formulation of the  $\overline{\mathbf{R}(\mathbf{U})}$ , readers can refer to Wang and di Mare [14] for details.

### Evaluation of Deterministic Fluxes

If the flow perturbations are already available by solving Equation 13, DF can be computed as the following. Equation 17 shows the DF in the convective fluxes, and if the triple terms (e.g.  $\overline{\rho' u_i'' u_j''}$  and  $\overline{\rho'' u_i'' H''}$ ) are ignored, DF can be written as:  $\overline{\rho u_i'' u_j''} \approx \bar{\rho} \overline{u_i'' u_j''}$  and  $\overline{\rho u_i'' H''} \approx \bar{\rho} \overline{u_i'' H''}$ .

It can be seen that computing DF requires the passage-mean of the correlation of two flow perturbations. Given the flow perturbations in the form of Fourier modes, this can be formulated as [23]:

$$\overline{\phi'' \psi''} = 2 \sum_{l=1}^{l=N_h} \left[ \text{Re}(\hat{\phi}_l) \text{Re}(\hat{\psi}_l) + \text{Im}(\hat{\phi}_l) \text{Im}(\hat{\psi}_l) \right] \tag{19}$$

$l$  is the harmonic index,  $N_h$  is the number of harmonics.  $\phi$  and  $\psi$  are dummy variables.

In terms of implementation, for a cell-centered finite volume solver, DF are computed in the cell center, interpolated to the interfaces with neighbouring cells using inverse-distance weighting interpolation, and accumulated to the right hand side. This is described in Equation 20 and also illustrated in Fig. 2. The shaded area represents control volumes.  $A$  is the area of the cell interface.  $d_L$  and  $d_R$  are

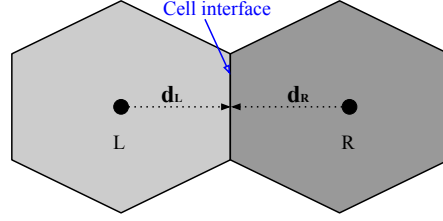


**FIGURE 2.** Illustration of computing DF on the cell interface in a cell-centered finite volume solver.

the distance from the cell center to the cell interface. For an edge-based finite volume solver, the weight of DF for the nodes sharing the edge reduces to 0.5.

$$DF_f = A \left( DF_L \frac{1/d_L}{1/d_L + 1/d_R} + DF_R \frac{1/d_R}{1/d_L + 1/d_R} \right) \quad (20)$$

## Mesh Generation

The computation of  $\mathbf{G}_k$  in Equation 9 requires  $\Delta \mathbf{x}_k$ . This can be computed by taking the difference of the coordinates of the mesh for the assembly with geometry variation and the one with the nominal geometry. Both meshes should have exactly the same topology, so structured mesh is preferred in this case. In this work, the in-house multi-block meshing tool [24] is used. The meshing tool firstly generates an algebraic mesh, which might have severe grid folding, and the mesh is then passed to an elliptic smoother to remove grid folding and generate boundary layer meshes. This process is illustrated in Fig. 3. In the current work, the grid points on the inlet/exit and periodic boundaries are fixed when the mesh is re-generated due to geometry variation..

## Boundary Conditions

The setup of the boundary conditions for the mean flow is the same as a typical single passage computation. so the focus here is for the linearized flow. For the linearized solution, the flow perturbations on the freestream boundaries (e.g. inlet and exit) are set to zero, since the flow perturbation is caused by grid displacement, which is embodied as the source term  $\hat{\mathbf{G}}_1$  in Equation 5. The periodic and wall boundaries are handled as the following ways:

**Periodic Boundary** For the linearized solver of the flow perturbation (i.e. Equation 13), a phase shift is applied on the lower periodic boundary and the resulting values are applied to the upper periodic boundary. If the IBPA  $\sigma$  is known, this can be formulated as:

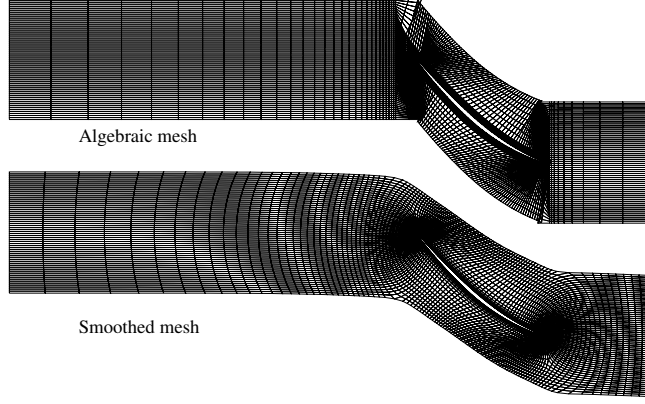


**FIGURE 3.** Algebraic mesh and elliptically smoothed mesh

$$\hat{\mathbf{U}}_{upper} = \hat{\mathbf{U}}_{lower} e^{l\sigma} \quad (21)$$

Since there is no spectral source terms in Equation 13, the coupling of the real part and the imaginary part of the flow perturbations only happens on the periodic boundaries via the phase shift term  $e^{l\sigma}$ .

**Viscous Wall** The mean flow and the linearized solver for the flow perturbation both use non-slip wall boundary conditions. Automatic wall treatment is used in the mean flow [25]. At each iteration,  $y^+$  is computed for the first cell on the wall and the wall shear stress is computed, which depends on whether the  $y^+$  is larger than 11 (wall function) or smaller than 11 (viscous sublayer). The linearized flow uses the  $y^+$  from the mean flow to compute the linearized wall shear stress on the wall. If  $y^+$  is larger than 11, the linearized wall function is used, otherwise the linearized viscous sublayer is used instead.

### Solution Procedure

The general procedure of the spectral method is demonstrated in Fig. 4. The inputs are the boundary conditions, the mesh of the passage-averaged or nominal geometry, and  $\Delta \mathbf{x}_k$ . The process starts from computing  $\hat{\mathbf{G}}_l$ , Equation 13 is then solved to obtain the flow perturbations in the form of Fourier modes. The deterministic fluxes are then computed and added to the mean flow computation. The mean flow (i.e. Equation 14) is finally updated with DF included. The above process repeats until certain convergence is met. A few variants can be derived from the above process and they are described below.

In the following text, the Spatial Favre-averaged Non-Linear Harmonic (SFNLH) method refers to the procedure illustrated in Fig. 4.  $\hat{\mathbf{G}}_l$  is re-computed whenever the mean flow is updated. It is noted that the cost of computing  $\hat{\mathbf{G}}_l$  is relatively high, especially as the engine

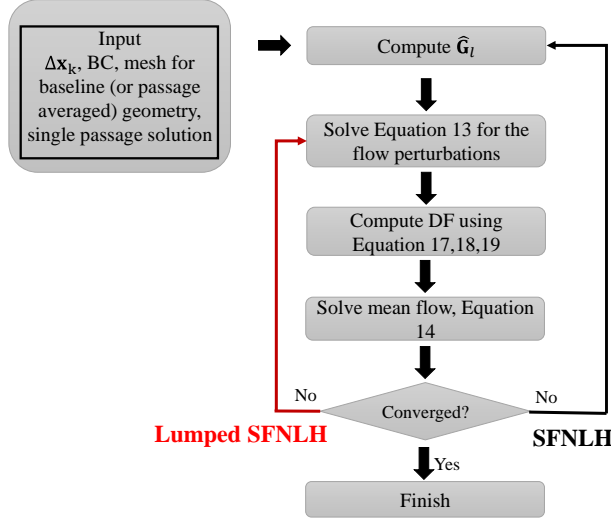


**FIGURE 4.** Flow chart of the spectral method

order of the geometry non-uniformity increases, as more passages are required for the spatial Fourier transform.

However, based on the experience that the passage-averaged flow in an assembly is generally similar to the single-passage flow.  $\hat{G}_l$  can be computed only once at the beginning of the computation using the single passage solution and frozen in the following procedure. In this following text, this approach is called lumped SFNLH and is illustrated in Fig. 4.

Furthermore, if DF is not included in the mean flow, this means there is no non-linear coupling between the flow perturbations and the passage-averaged flow. The mean flow reduces to the single passage flow. This approach is called Spatial Linear Harmonic (SLH) method in the following text.

The performance of SLH, SFNLH, and lumped SFNLH will be examined in the paper and their performance on different levels of flow perturbations are discussed.

## Computational Cost

Assume the computational cost of a single passage steady simulation is 1, the computational cost of computing  $N_h$  harmonics is roughly  $2N_h+1$ .  $2N_h$  is the computational cost of the real and imaginary parts of  $N_h$  harmonics and 1 is the one for the mean flow. There is also extra cost to compute  $\hat{G}_l$ . For SLH and lumped SFNLH, they can be computed only once at the beginning and their computational cost is negligible. For SFNLH, considering the fact that the difference of the passage-averaged flow is similar to the single passage flow,  $\hat{G}_l$  can be updated every 10-30 pseudo time steps, its cost can be reduced to a fraction of the one for a single passage steady solution. Compared to a whole assembly steady simulation, the reduction of computational cost  $r_{\text{cost}}$  can be estimated as:

$$r_{\text{cost}} \approx \frac{N}{2N_h + 1 + C_G} \quad (22)$$

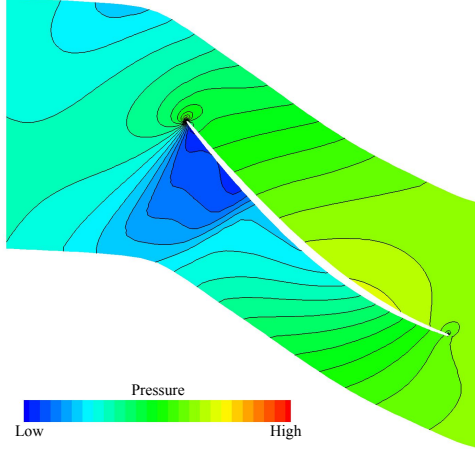


**FIGURE 5.** Pressure distribution in the fan passage

$N$  is the number of passages in the assembly.  $C_G$  is the computational cost to compute  $\hat{\mathbf{G}}_l$ . To compute one harmonic, for an OGV assembly with roughly 40 passages, if we assume  $C_G \approx 0.2$ ,  $r_{\text{cost}} = 12.5$ ; For a fan assembly with roughly 20 passages,  $r_{\text{cost}} = 6.25$ . It is noted that the advantage of the spectral method diminishes with reduced number of passages and increased number of harmonics to compute in the simulation.

### CFD Solver

The CFD solver used in this paper is the in-house code AU3X [26,27]. AU3X uses the cell-centered finite volume scheme to solve the steady/unsteady RANS equations on unstructured meshes with implicit matrix-free method. The code is second-order accurate in space and time. Second-order convective fluxes are computed by Roe's approximated Riemann solver and Monotonic Upwind Scheme for Conservation Law (MUSCL) is used for the upwind fluxes with the van Albada limiter. The code has also been optimized on modern multi-core and many-core architectures [28].

### Case Studies

The performance of the spectral method is assessed on a modern fan assembly in a ultra high bypass ratio jet engine for long haul service. The number of passages in the fan assembly is 18. Blade re-staggering with low EO and 9EO are examined using the spectral method and compared with the direct whole assembly solution. Typical flow feature in the fan assembly features the shock in the passage towards the tip. This is illustrated in Fig. 5, which shows the pressure distribution of the single passage solution around 75% span. It is noted that the inlet has been extended in the computations, as is shown in Fig. 3. The domain shown in Fig. 5 is truncated.

Two set of cases are presented to validate the spectral method on the fan assembly. A detailed parametric study is firstly performed in a quasi-3D simulation of the 75% span of the fan blade to demonstrate the performance of different variants of the spectral methods

**TABLE 1.** Summary of case studies

	stagger variation	1EO	2EO	9EO
Quasi 3D	0.1°	✓	✓	✓
	0.2°	✓	✓	✓
	0.3°			✓
	0.4°			✓
3D	0.4°	✓	✓	✓

**TABLE 2.** Setup of the spectral method

	IBPA	Frequency
1EO	$\frac{\pi}{9}$	0
2EO	$\frac{2\pi}{9}$	0
9EO (“saw-tooth”)	$\pi$	0

using stagger variability of different angles and engine order. The most cost-effective one is then used to perform a fully 3D simulation of the fan blade to demonstrate the capability of the method to handle 3D flows. The test cases are summarized in Table 1.

Regarding to setting up the spectral method, Table 2 shows the setup of the linear solver (i.e. Equation 13). The frequency is zero, which means the flow perturbation due to geometry variation is a stationary flow disturbance in the rotor frame of reference. The IBPAs for 1EO, 2EO and 9EO are  $\pi/9$ ,  $2\pi/9$  and  $\pi$  respectively.

The amount of stagger variation is comparable to the values reported by Wilson et al [15] and this is summarized in Table 1. As will be shown in the following test cases, the spectral methods perform better on low EO stagger variation under the same re-stagger angle, more focuses are on 9EO cases to demonstrate the capability of the method to handle flow non-linearity.

### Case 1: Quasi-3D Simulation at 75% span

#### Low EO Geometry Distortion

In the first place, 1EO and 2EO stagger variations are considered. The relative re-stagger angle to the mean geometry is shown in Fig. 6. The maximum re-stagger angle is 0.2°. As fan blades have large chord-thickness ratio, a 0.2° of re-staggering can lead to a appreciable amount of displacement of the blade leading/trailing edges, which is comparable to the blade thickness.

A mesh sensitivity study is performed on the 1EO stagger variation. Three meshes are prepared. The coarse mesh has 11296 cells, the medium mesh has 17476 cells and the fine mesh has 21450 cells. The computed pressure distribution and the Fourier transform of the pressure perturbation on the blade are shown in Fig. 7. The results for both the mean flow and the Fourier solutions are close between the medium and the fine meshes. The medium mesh is used in the following study.

The pressure of the mean flow is normalized by the largest pressure on the blade. The real and imaginary part of the pressure

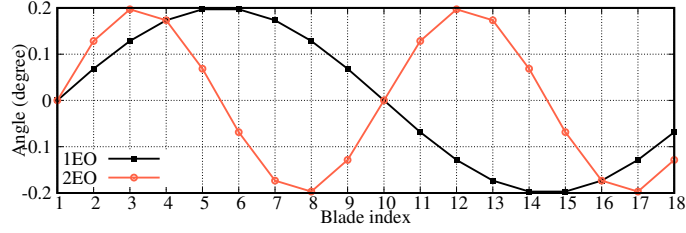


**FIGURE 6.** Re-stagger angle for each angle with 1 harmonic and 2 harmonics

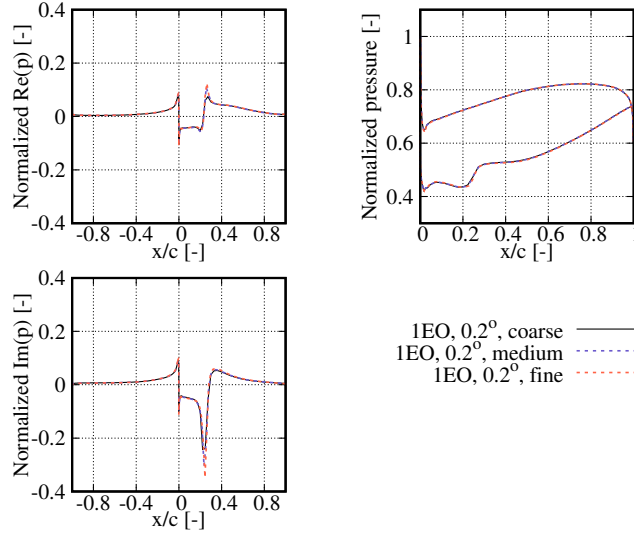


**FIGURE 7.** Grid sensitivity study. Left: Fourier-transformed pressure perturbation on the blade. Right: pressure distribution on the blade in the mean flow.

perturbation is normalized by a reference pressure, which is taken as the largest magnitude of the pressure perturbation when the fan assembly has a re-staggering angle  $0.2^\circ$  with “saw-tooth” pattern. In all the quantitative comparisons of pressure perturbation, if not stated explicitly, their real and imaginary parts are normalized by this value. The rationale of this normalization is that one can observe how pressure perturbation changes with EO and re-stagger angle if either of them varies.

Since there are 18 passages in the assembly, it is cumbersome to compare the flow field for each passage. Instead the whole assembly solution is Fourier-transformed and compared with the spectral solutions. With the fan blade under 1EO distortion, Figure 8 shows the real and imaginary parts of the pressure perturbations in the fan passage under 1EO stagger variation. It can be seen that qualitatively SFNLH has a good agreement with the direct assembly solutions. Due to the re-staggering of the blade, the shock in the fan passage also moves harmonically. The shock movement also changes the potential field upstream of the leading edge and contributes to the generation of multiple tone noise.

Figure 9 shows the pressure perturbations on the blade with 1EO and 2EO stagger variations, respectively. Direct whole assembly, SFNLH, SLH and lumped SFNLH solutions are compared with each other. It can be seen that SLH has excellent agreement with the

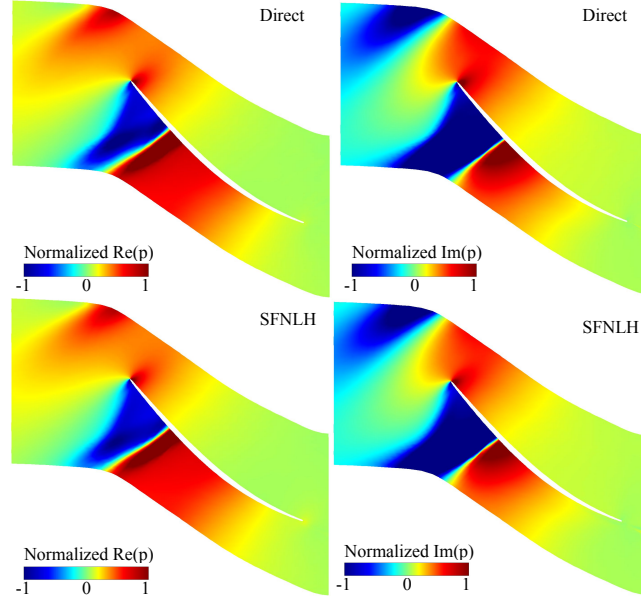


**FIGURE 8.** Pressure perturbations in the fan passage under 1EO geometry distortion.

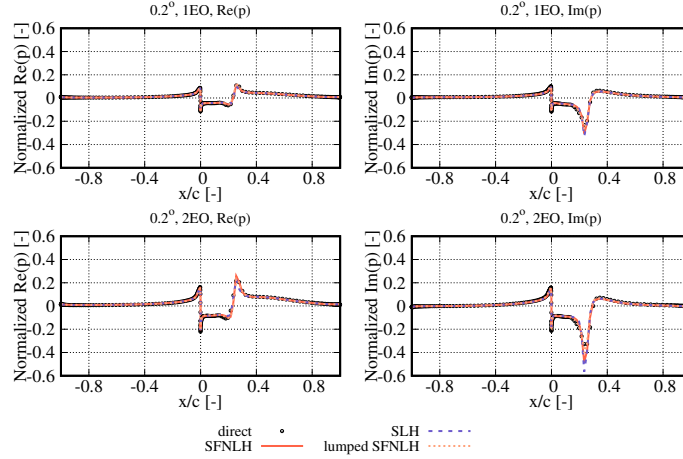


**FIGURE 9.** Pressure perturbations on the blade with 1EO and re-staggering angle  $0.2^\circ$

direct whole assembly solution. The largest discrepancy is observed around 25% chord, where the shock is located and the flow is strongly non-linear. Including deterministic fluxes improves the prediction of the pressure variations around this region. The lumped SFNLH solution is found to be very close to the SFNLH solution, so it is a cost-effective alternative to SFNLH.

As is shown in Fig. 8, the shock pattern in front of the fan leading edge will be changed due to stagger variations, and contribute to the generation of multiple tone noise. The pressure perturbation roughly 10% upstream of the fan leading edge is plotted along the pitch-wise direction and this is shown in Fig. 10. It can be seen that there is good agreement between the solutions from spectral methods (i.e. SLH, SFNLH, lumped SFNLH) and the direct whole assembly solution.



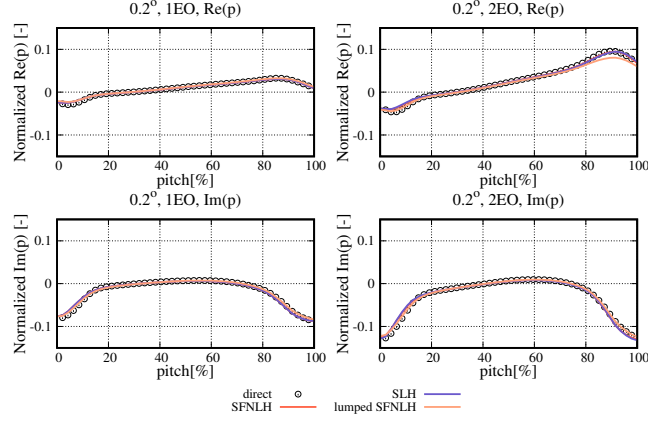


**FIGURE 10.** Pressure perturbation 10% upstream of the fan leading edge with 1EO and 2EO geometry distortion

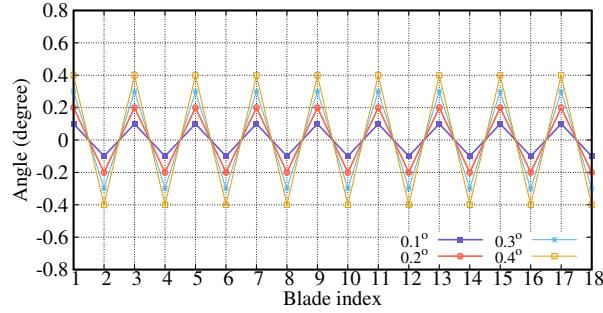


**FIGURE 11.** Re-stagger angle for “saw-tooth” pattern

## The “Saw-Tooth” Pattern

The “saw-tooth” pattern in a fan assembly is the scenario that the relative re-staggering angle of neighbouring blades have the same value but opposite sign. This phenomenon originates from a mis-stagger of a single blade and the “saw-tooth” pattern is then developed at intermediate flow conditions. Such a situation could lead to sustained vibration and consequentially fatigue damage. Wilson et al [15] had a detailed discussion of this and attentive readers can refer to [15] for more details. Here our purpose is to assess the performance of the spectral methods to predict the flow fields (e.g. pressure) in the fan assembly with this pattern.

The relative re-staggering angle in this study is illustrated in Fig. 11. The “saw-tooth” pattern essentially represents a 9EO stagger variation with an inter-blade phase angle of  $\pi$ . It can also be seen that the wave number of the signal is the Nyquist wave-number, and the spectral method suffice to capture the signal without aliasing issues. A parametric study is performed here to examine the performance of the spectral methods for a set of angles. The magnitudes of the re-staggering are set to  $0.1^\circ$ ,  $0.2^\circ$ ,  $0.3^\circ$ , and  $0.4^\circ$  respectively. The choice of these angles is based on the values reported by Wilson et al [15].

The Fourier-transformed pressure perturbation is shown in Fig. 12. The signals in Fig. 11 are cosine waves with an IBPA of  $\pi$  between neighbouring passages. The Fourier-transform of the whole assembly solution shows that the imaginary part is very small, therefore only the real part is shown here. Furthermore since the IBPA is  $\pi$ , the pressure of the neighbouring passage can be easily

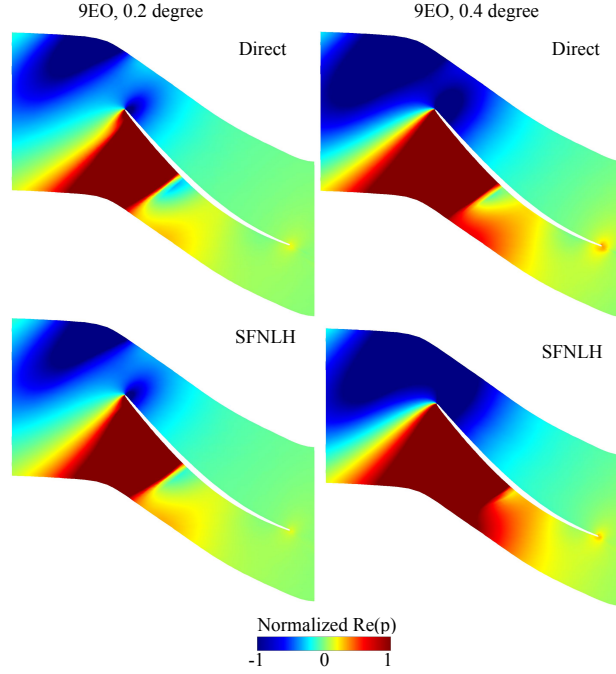


**FIGURE 12.** Real part of the pressure perturbation for 9EO with  $0.2^\circ$

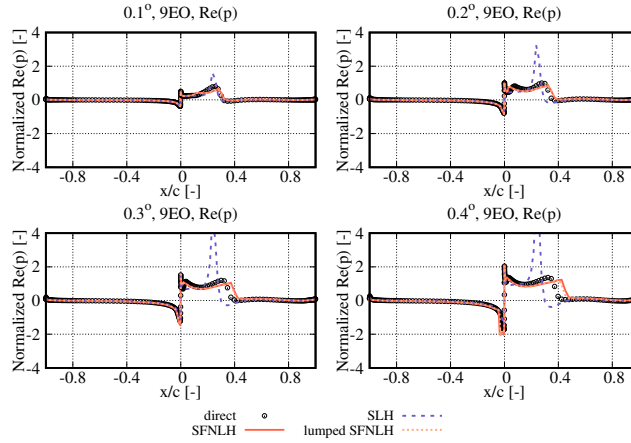


**FIGURE 13.** Real part of perturbation variation on the blade for 9EO pattern

produced by simply changing the sign of the pressure variation of the current passage.

The real part of the Fourier transformed perturbation for  $0.2^\circ$  and  $0.4^\circ$  are qualitatively compared between SFNLH and direct whole assembly solutions, and this is shown in Fig. 12. It can be seen that there is a good agreement between SFNLH and the direct whole assembly solution.

Quantitative comparison of Fourier transformed pressure perturbation is shown in Fig. 13, and it shows good agreement with the direct whole assembly solutions when re-staggering angles are  $0.1^\circ$ ,  $0.2^\circ$ ,  $0.3^\circ$  and  $0.4^\circ$  respectively. It can be seen that as the re-

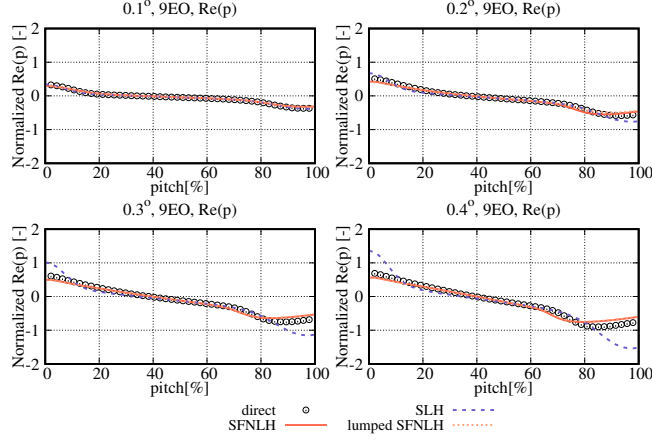


**FIGURE 14.** Real part of pressure perturbation 10% upstream the blade leading edge, 9EO pattern

staggering angle increases, there are larger pressure perturbations on the blade surface and the discrepancies between the spectral methods and the direct whole assembly also increases especially around the region where the shock is located. This is because the spectral method is built upon the linear correlation between grid displacement and flow perturbations (see Equation 5), as flow perturbations becomes larger, such assumption becomes less accurate.

Compared to low EO cases, SLH performs poorly in 9EO cases and the pressure variation is over-predicted on the suction side. On the pressure side, it has good agreement with the direct whole assembly solution, which strongly indicates that there is a linear response of pressure variation to grid displacement on the pressure side for both low EO and high EO stagger variations. With deterministic fluxes included, SFNLH has improved agreement with the direct whole assembly solution.

Lumped SFNLH shows similar results to SFNLH but demands less computational cost. Since the “saw-tooth” pattern is a 9EO geometry distortion, a full sampling is always required, which is expensive to compute at each iteration. As is mentioned before, the computation of  $\hat{\mathbf{G}}_l$  is skipped every 10-30 time steps to offset its extra computational cost. For lumped SFNLH,  $\hat{\mathbf{G}}_l$  is computed only once at the start of the computation. Therefore lumped SFNLH is a more cost-effective tool compared to SFNLH for the fan assembly with high EO distortions.

The potential field in front of the leading edge is also examined. The data in the pitch-wise direction is extracted roughly 10% upstream the leading edge and is shown in Fig. 14. As is explained before, since the imaginary part is small, only the real part is shown. There is better agreement with direct whole assembly solutions compared to the pressure perturbation on the blade, especially for SFNLH and lumped SFNLH. This is because there is less flow non-linearity in this location, which is favourable to a linearized NS solver. It is also clear that as re-staggering angle increases, there are larger perturbations in the potential field and this trend is captured well quantitatively by all the spectral methods.

## Remarks on SLH, SFNLH and lumped SFNLH

The above parametric studies in low EO and 9EO stagger variations show that with the same re-staggering angle, increasing the EO of the stagger variation will lead to larger flow perturbations. This can be observed by comparing Fig. 9 and Fig. 13. This is because increasing the EO of stagger variation will lead to larger geometry difference of neighbouring blade passages, this will result in bigger changes in the passage area and then lead to larger flow perturbations. Furthermore, it is obvious that with the same EO of stagger variation, increasing the re-staggering angle will lead to larger flow perturbations.

It is noted that there are two sets of non-linearity in the flow field of an assembly with non-uniform geometries. The first one is the non-linear relationship between grid displacement and flow perturbations. The second one is the non-linear coupling between the passage-averaged flow and the flow perturbations. The first non-linearity is approximated by a linear relationship shown in Equation 5 and the high order terms are ignored. The second non-linearity, which is the non-linear coupling between the passage-averaged flow and the flow perturbations, are realized through the inclusion of DF in the mean flow (see Equation 14).

SLH only solves Equation 13 and it represents a linear analysis. As flow perturbations become larger, its accuracy degrades. This can be observed in cases with larger re-staggering angle and higher EO. SFNLH solves the passage-mean flow (Equation 14) and the linearized flow together, so SFNLH performs better than SLH when there are larger flow perturbations. However SFNLH is more expensive than SLH, since it requires to compute the source term  $\hat{\mathbf{G}}_l$ . Lumped SFNLH represents a hybrid of SLH and SFNLH. Lumped SFNLH retains the accuracy of SFNLH but with the computational cost similar to SLH. It can be seen from the above parametric study that lumped SFNLH represents the most cost-effective spectral approach and it will be used in the following full 3D simulations.

## Case 2: Full 3D Simulation

It is known that the variation of the stagger angle in a fan assembly is the dominant geometric feature to generate the multi-tone noise, also referred as buzz-saw noise. As is pointed out by Gliebe et al [29], stagger angle difference as small as  $0.1^\circ$  could lead to substantial multiple tone noise. These noises share the same fundamental frequency, which is the blade passing frequency, but there are sub-harmonics, which is due to the stagger variation in the fan assembly.

The 3D geometry of the fan assembly is shown in Fig. 15, and the 3D simulation is to demonstrate the capability of the spectral method to predict the pressure perturbations upstream the fan assembly when it is under 1EO, 2EO and 9EO stagger variations. The data are examined in a plane which is denoted by the blue dashed line in Fig. 15. The plane is sitting upstream the fan leading edge and it is roughly 20% of the mid-span chord upstream the mid-span leading edge. The setup of the spectral method is identical to the quasi-3D simulations, as is shown in Table 2. It is demonstrated in the quasi-3D simulations that lumped SFNLH is the most cost-effective approach, therefore it is used here to perform the 3D simulations and compared with direct whole assembly solutions.

The pressure field upstream the fan assembly can be decomposed as a passage-averaged value, which has the periodicity of the pitch of the nominal geometry, and also a perturbation  $\Delta p$ . For an observer in the stationary frame of reference, the passage-mean value

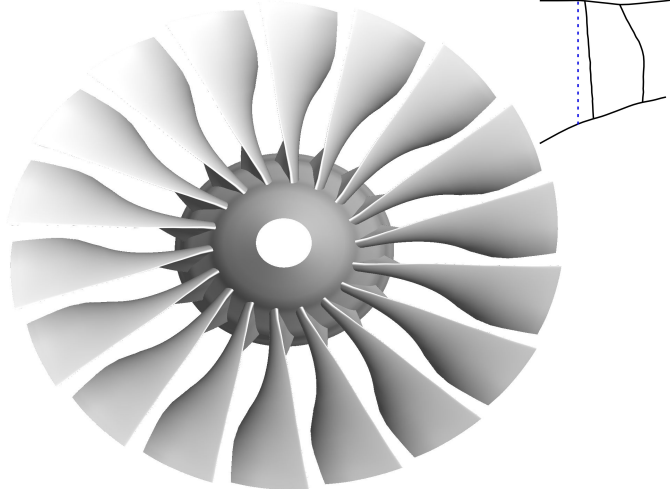


**FIGURE 15.** 3D Geometry of the fan assembly. The figure has been intentionally distorted.

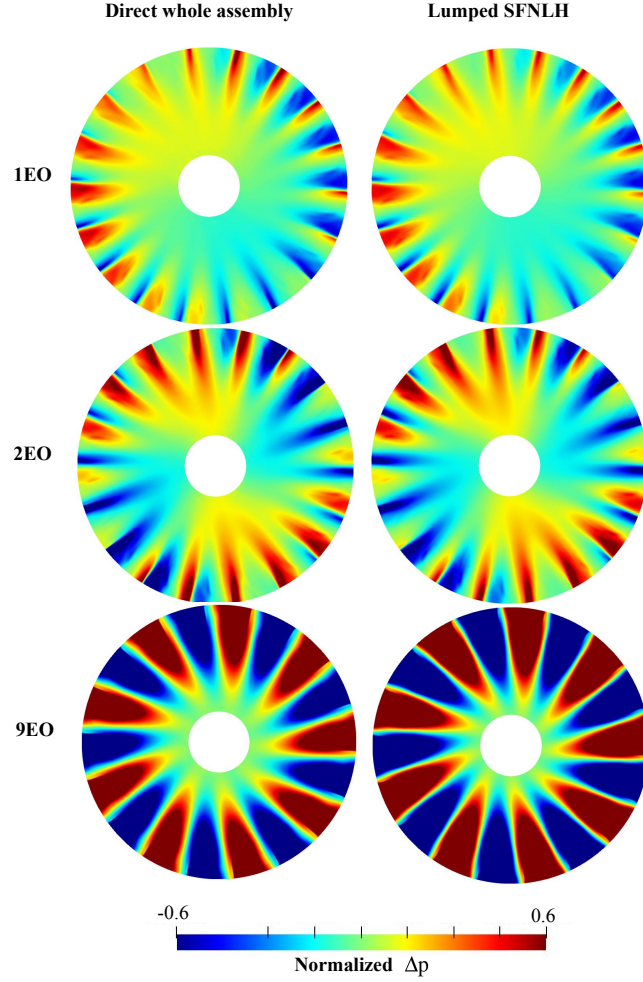
contributes to the tonal noise and  $\Delta p$  is the sub-harmonics due to stagger variation and leads to the multiple tone noise.

Figure 16 shows the distribution of  $\Delta p$  for 1EO, 2EO and 9EO stagger variation and the magnitude of the re-staggering is  $0.4^\circ$ . The data is extracted on the plane illustrated in Fig. 15. The values have been normalized by the largest  $\Delta p$  at 90% span. There is good agreement between the direct whole assembly solution and lumped SFNLH solution, especially for 1EO and 2EO re-staggering. It can be seen that  $\Delta p$  is much larger towards the casing. This is mainly due to the fact that the flow towards the hub is subsonic, and the pressure disturbance decays exponentially upstream.

Detailed quantitative comparisons on 25%, 50% and 90% spans are shown in Fig. 17, Fig. 18 and Fig. 19. The figures show that there are generally good agreement with the direct whole assembly solution from the 25% to 90% span. For the case of 9EO re-staggering, the accuracy of the spectral method degrades slightly. As is demonstrated in the quasi-3D simulations, 9EO re-staggering leads to the largest flow perturbations compared to low EO ones. The discrepancy is due to the linear assumption (i.e. Equation 6), which correlates the grid displacement and flow perturbations. As the flow perturbations becomes increasingly larger, such linear assumption becomes less accurate. This trend can also be observed in Fig. 13.

### Remarks on Computational time

Considering the reduction in terms of wall-clock time using the spectral method,  $r_{\text{cost}}$  (see Equation 22) is the maximum speed up one can achieve compared to direct whole assembly simulations. The actual speedup strongly depends on the implementation of solving Equation 13. In the current implementation, the mean flow is solved implicitly with Newton-Jacobi and the linearized flow (i.e. Equation 13) is solved explicitly with Runge-Kutta. This is less optimal and only 30% to 50% of the theoretical speed-up are achieved in the current implementation. For the studied fan assembly with 18 passages, the actual speed-up is a factor of 2 to 3 in the current implementation. Nonetheless, the focus of this paper is to demonstrate the correctness and accuracy of the spectral method. There are a



**FIGURE 16.** Distribution of pressure perturbation with 1EO, 2EO and 9EO stagger variation.

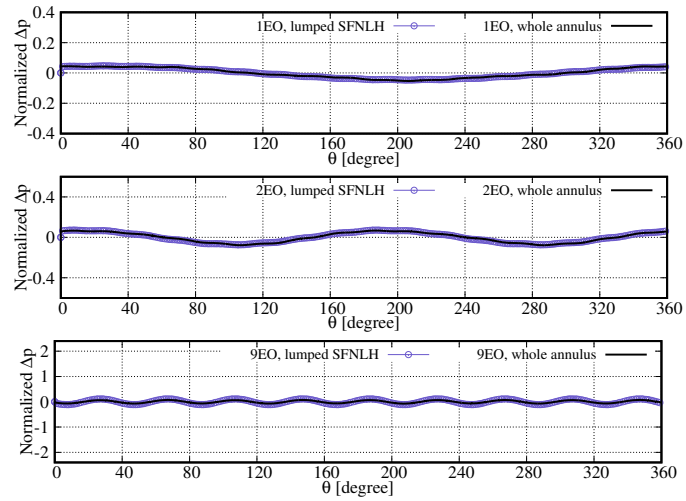


**FIGURE 17.** Circumferential distribution of pressure disturbance  $\Delta p$  at 25% span with 1EO, 2EO and 9EO stagger variations.

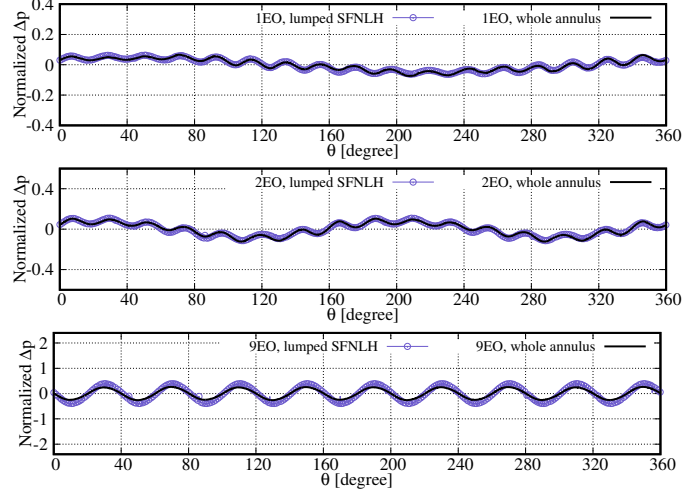


**FIGURE 18.** Circumferential distribution of pressure disturbance  $\Delta p$  at 50% span with 1EO, 2EO and 9EO stagger variations.

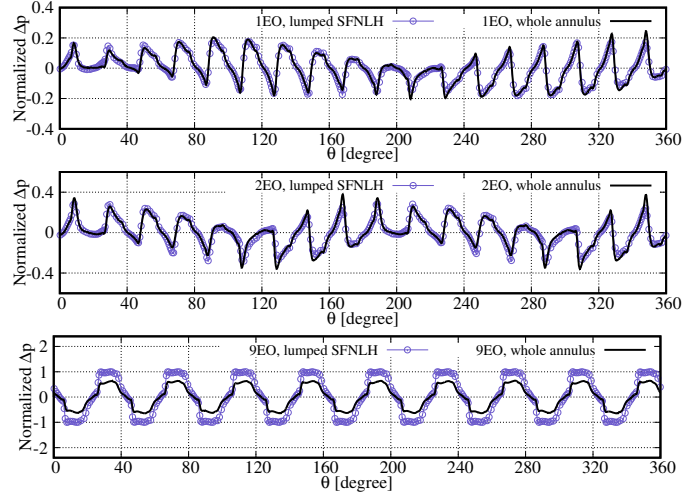


**FIGURE 19.** Circumferential distribution of pressure disturbance  $\Delta p$  at 90% span with 1EO, 2EO and 9EO stagger variations.

range of acceleration techniques, such as multigrid or Newton-Krylov methods [30], which can be used to accelerate the convergence. Future work is to address this issue.

## Conclusions and Future Work

This paper has presented a procedure to analyze fan assemblies with stagger variations using spectral methods. Parametric studies of low EO and 9EO restaggering are performed and the solutions from the spectral methods are compared with the corresponding direct whole assembly solutions. Generally good agreement is observed. The spectral method reproduces the correct scaling of the observed flow distortions with respect to the magnitude of the geometry perturbations and with respect to their wave length. The method can be easily implemented into existing harmonic flow solvers by including the source term  $\hat{\mathbf{G}}_l$ .

The effect of deterministic fluxes on the prediction of flow perturbations is studied parametrically in the quasi-3D simulations. From the cases of low EO and 9EO, it can be seen that the effect of deterministic fluxes become increasingly important as the flow perturbations become larger. Care should be taken if a pure linear analysis, i.e. SLH, is used for cases with large flow perturbations. Lumped SFNLH can be a good alternative to SFNLH where possible, since one only needs to compute the vector  $\hat{\mathbf{G}}_l$  once at the beginning and is computationally cheaper than SFNLH which updates  $\hat{\mathbf{G}}_l$  regularly during the computation.

The 3D simulation shows good agreement between lumped SFNLH and direct whole assembly solutions on both low EO and 9EO stagger variations. The performance of the spectral method is consistent with the one observed in quasi-3D simulations. This case also demonstrates the potential of the current method to be an efficient tool to predict multiple tone noise generations.

Future work is planned towards increasing the accuracy and computational efficiency of the spectral method. The accuracy of the current spectral method degrades as the flow perturbation due to geometry non-uniformity increases. Future work is to include the non-linear coupling of the flow perturbation and grid displacement to improve the accuracy. Besides, the linearized flow needs to be solved more efficiently to improve the computational efficiency of the spectral method.

## ACKNOWLEDGMENT

The authors are grateful to Rolls-Royce plc for funding this work and granting permission for its publication. The authors would also like to thank Dr. John Adamczyk for his suggestions on this work.

## NOMENCLATURE

### Latin symbols

- $c$  axial chord
- $C_G$  normalized computational cost to evaluate  $\hat{\mathbf{G}}_l$
- $d$  distance
- $\mathcal{F}$  spatial Fourier transform operator
- $\mathbf{G}$  right hand side for the linearized flow with respect to grid displacement
- $I$  imaginary unit,  $\sqrt{-1}$
- $N$  number of passages
- $N_h$  number of harmonics
- $u$  velocity
- $U$  conservative variable
- $p$  pressure
- $\mathbf{R}$  residual



$t$  time

### **Greek symbols**

$\rho$  density

$\tau$  time

$\phi$  dummy flow variable

$\psi$  dummy flow variable

### **Subscripts, superscripts and operators**

$f$  cell interface

$i$  spatial index

$j$  spatial index

$k$  space navigation index

$l$  Fourier index

$L$  Left

$R$  Right

$'$  fluctuation relative to the passage-averaged quantity

$''$  fluctuation relative to the Favre-averaged quantity

$-$  passage-average

$\sim$  Favre-average

$\wedge$  Fourier coefficient

### **Acronym**

CFD Computational Fluid Dynamics

DF Deterministic Flux

EO Engine Order

HB Harmonic Balance

IBPA Inter-Blade Phase Angle

Im imaginary part of a complex number

NLH Non-Linear Harmonic

NS Navier-Stokes

Re Real part of a complex number

SFNLH spatial Favre-averaged Non-Linear Harmonic

SLH spatial Linear Harmonic

OGV Outlet Guide Vane

PS Pressure Side

RANS Reynolds-Averaged Navier-Stokes

URANS Unsteady Reynolds-Averaged Navier-Stokes

SS Suction Side

## REFERENCES

- [1] Hall, K. C., and Crawley, E. F., 1989. "Calculation of unsteady flows in turbomachinery using the linearized Euler equations". *AIAA Journal*, **27**(6), June, pp. 777–787.
- [2] He, L., and Ning, W., 1998. "Efficient approach for analysis of unsteady viscous flows in turbomachines". *AIAA Journal*, **36**(11), Nov., pp. 2005–2012.
- [3] Adamczyk, J. J., 1999. "Aerodynamic analysis of multistage turbomachinery flows in support of aerodynamic design". *Journal of Turbomachinery*, **122**(2), Feb., pp. 189–217.
- [4] Wang, F., and di Mare, L., 2019. "Favre-averaged nonlinear harmonic method for compressible periodic flows". *AIAA Journal*, **57**(3), Mar., pp. 1133–1142.
- [5] Hall, K. C., Thomas, J. P., and Clark, W. S., 2002. "Computation of unsteady nonlinear flows in cascades using a harmonic balance technique". *AIAA Journal*, **40**(5), May, pp. 879–886.
- [6] McMullen, M., and Jameson, A., 2006. "The computational efficiency of non-linear frequency domain methods". *Journal of Computational Physics*, **212**(2), Mar, pp. 637–661.
- [7] Sicot, F., Puigt, G., and Montagnac, M., 2008. "Block-jacobi implicit algorithms for the time spectral method". *AIAA Journal*, **46**(12), Dec, pp. 3080–3089.
- [8] Hall, K. C., Ekici, K., Thomas, J. P., and Dowell, E. H., 2013. "Harmonic balance methods applied to computational fluid dynamics problems". *International Journal of Computational Fluid Dynamics*, **27**(2), Feb, pp. 52–67.
- [9] Vasanthakumar, P., 2003. "Three dimensional frequency-domain solution method for unsteady turbomachinery flows". Phd thesis, Durham University, Durham, UK, Jan.
- [10] Vilmin, S., Lorrain, É., Tartinvill, B., Capron, A., and Hirsch, C., 2013. "The nonlinear harmonic method: from single stage to multi-row effects". *International Journal of Computational Fluid Dynamics*, **27**(2), Feb, pp. 88–99.
- [11] Wang, F., di Mare, L., and Adami, P., 2019. "Favre-averaged fourier-based methods for gas turbine flows". In Volume 2C: Turbomachinery, American Society of Mechanical Engineers.
- [12] He, L., 2010. "Fourier methods for turbomachinery applications". *Progress in Aerospace Sciences*, **46**(8), Nov., pp. 329–341.
- [13] He, L., 2006. "Fourier modeling of steady and unsteady nonaxisymmetrical flows". *Journal of Propulsion and Power*, **22**(1), jan,

pp. 197–201.

- [14] Wang, F., and di Mare, L., 2019. “Efficient approach for simulating aperiodic flows due to geometry distortions”. *AIAA Journal*, Dec., pp. 1–14.
- [15] Wilson, M. J., Imregun, M., and Sayma, A. I., 2006. “The effect of stagger variability in gas turbine fan assemblies”. *Journal of Turbomachinery*, **129**(2), June, pp. 404–411.
- [16] Hoyniak, D., and Fleeter, S., 1986. “Forced response analysis of an aerodynamically detuned supersonic turbomachine rotor”. *Journal of Vibration and Acoustics*, **108**(2), Apr., pp. 117–124.
- [17] Hoyniak, D., and Fleeter, S., 1986. “Aerodynamic detuning analysis of an unstalled supersonic turbofan cascade”. *Journal of Engineering for Gas Turbines and Power*, **108**(1), Jan., pp. 60–67.
- [18] Hawkings, D., 1971. “Multiple tone generation by transonic compressors”. *Journal of Sound and Vibration*, **17**(2), July, pp. 241–250.
- [19] STRATFORD, B., and NEWBY, D., 1977. “A new look at the generation of buzz-saw noise”. In 4th Aeroacoustics Conference, American Institute of Aeronautics and Astronautics.
- [20] Han, F., Sharma, A., Paliath, U., and Shieh, C., 2014. “Multiple pure tone noise prediction”. *Journal of Sound and Vibration*, **333**(25), Dec., pp. 6942–6959.
- [21] Lu, Y., Lad, B., Vahdati, M., and Stapelfeldt, S. C., 2019. “Nonsynchronous vibration associated with transonic fan blade untwist”. In Volume 7A: Structures and Dynamics, American Society of Mechanical Engineers.
- [22] He, L., 2008. “Harmonic solution of unsteady flow around blades with separation”. *AIAA Journal*, **46**(6), June, pp. 1299–1307.
- [23] Vilmin, S., Lorrain, E., Hirsch, C., and Swoboda, M., 2006. “Unsteady flow modeling across the rotor/stator interface using the nonlinear harmonic method”. In Volume 6: Turbomachinery, Parts A and B, ASMEDC.
- [24] Wang, F., and di Mare, L., 2017. “Mesh generation for turbomachinery blade passages with three-dimensional endwall features”. *Journal of Propulsion and Power*, **33**(6), nov, pp. 1459–1472.
- [25] F. R. Menter, M. K., and Langtry, R., 2003. “Ten years of industrial experience with the sst turbulence model”. In Proceedings of the 4th International Symposium on Turbulence, Heat and Mass Transfer, Begell House Inc., pp. 625–632.
- [26] di Mare, L., Kulkarni, D. Y., Wang, F., Romanov, A., Ramar, P. R., and Zachariadis, Z. I., 2011. “Virtual gas turbines: Geometry and conceptual description”. In Proceedings of ASME TurboExpo, Vancouver, Canada, ASME.
- [27] Wang, F., Carnevale, M., Lu, G., di Mare, L., and Kulkarni, D., 2016. “Virtual gas turbine: Pre-processing and numerical simulations”. In Proceedings of ASME TurboExpo, South Korea, Seoul, ASME.
- [28] Hadade, I., Wang, F., Carnevale, M., and di Mare, L., 2019. “Some useful optimisations for unstructured computational fluid dynamics codes on multicore and manycore architectures”. *Computer Physics Communications*, **235**, feb, pp. 305–323.
- [29] Gliebe, P., Mani, R., Shin, H., Mitchell, B., Ashford, G., Salamah, S., and Connel, S., 2000. Aeroacoustic prediction codes. Tech.

Rep. NASA/CR-2000-210244, NASA.

- [30] Saad, Y., and Schultz, M. H., 1986. “GMRES: A generalized minimal residual algorithm for solving nonsymmetric linear systems”. *SIAM Journal on Scientific and Statistical Computing*, 7(3), July, pp. 856–869.